

# Monitoring Fast, Voxel-Scale Cure Kinetics via Sample-Coupled-Resonance Photorheology

Callie I. Fiedler-Higgins,\* Lewis M. Cox, Frank W. DelRio, and Jason P. Killgore\*

Photopolymerizable materials are the focus of extensive research across a variety of fields ranging from additive manufacturing to regenerative medicine. However, poorly understood material mechanical and rheological properties during polymerization at the relevant exposure powers and single-voxel length-scales limit advancements in part performance and throughput. Here, a novel atomic force microscopy (AFM) technique, sample-coupled-resonance photorheology (SCRPR), to locally characterize the mechano-rheological properties of photopolymerized materials on the relevant reaction kinetic timescales, is demonstrated. By coupling an AFM tip to a photopolymer and exposing the coupled region to a laser, two fundamental photopolymerization phenomena: (1) timescales of photopolymerization at high laser power and (2) reciprocity between photodose and material properties are studied. The ability to capture rapid kinetic changes occurring during polymerization with SCRPR is demonstrated. It is found that reciprocity is only valid for a finite range of exposure powers in the verification material and polymerization is highly localized in a low-diffusion system. After polymerization, *in situ* imaging of a single polymerized voxel is performed using material-appropriate topographic and nanomechanical modalities of the AFM while still in the as-printed environment.

Additive manufacturing (AM), or 3D printing, is widely promoted as the next generation of agile, efficient manufacturing technology with the ability to fabricate complex structures for applications ranging from low-cost rapid prototyping to life-saving tissue engineering.<sup>[1]</sup> To build a structure, the desired 3D part file is “sliced” into discrete 2D sections that are used to iteratively build the part from a given material. As a result of layered fabrication, AM introduces microscale anisotropic heterogeneities in chemical, thermal, and mechanical properties such that the performance of parts depends strongly and often unpredictably on printing conditions.<sup>[2]</sup> Presently, light-based AM techniques afford unique combinations of throughput, resolution, and

performance. An array of light-based AM methods exist including nozzle-based systems, selective laser sintering, and stereolithography (SLA).<sup>[1e,2b,3]</sup> For light-based AM technology to be harnessed and improved, a fundamental understanding of material properties must be developed. Nonuniformities in a printed voxel, the smallest AM printing unit, arise from a variety of sources including: (1) nonuniform light intensity with depth due to Beer–Lambert absorption, (2) reactive species diffusion occurring at the same spatiotemporal scales as the polymerization reaction, and (3) nonlinear light-intensity-dependent polymerization.<sup>[2b,4]</sup> Because of these complex and often-competing phenomena, material properties throughout a given layer vary dynamically in space and time. This subsequently leads to uncharacterized, chemically and mechanically heterogeneous printed structures.<sup>[2d,5]</sup> Current techniques used to characterize as-printed AM objects, such as tensile and compressive stress testing, do not adequately represent the

structure because they inaccurately assume uniform, bulk mechanical properties.<sup>[2b,6]</sup> Furthermore, this as-printed characterization approach lends minimal insight into the time-dependent polymerization process that determines final part properties and regulates AM throughput. Oscillatory rheometry provides mechanical property testing during the photopolymerization process, but operates with second-scale temporal resolution and macroscale volumes, thus significantly missing the time and length scales of AM, which polymerizes microscale volumes in just milliseconds.<sup>[2b,4a]</sup> To characterize material *in situ*, researchers are forced to reduce light intensity until the reaction and measurement timescales match, then make unprovable assumptions about the reciprocity between light dosage and kinetics.<sup>[7]</sup> Ultimately, techniques to measure the rheological properties of AM voxels *in situ*, with the temporal resolution to capture the rapid kinetic events (<1 ms) must be used.<sup>[8]</sup> Here, we introduce a novel atomic force microscopy (AFM) technique, sample-coupled resonance photorheology (SCRPR) capable of measuring rheological changes during photopolymerization at millisecond timescales and subvoxel length scales, thus revealing direct characterization of fast kinetic timescales and challenging the validity of reciprocity assumptions.

Dr. C. I. Fiedler-Higgins, Dr. L. M. Cox, Dr. F. W. DelRio, Dr. J. P. Killgore  
Applied Chemicals and Materials Division  
National Institute of Standards and Technology  
325 Broadway, Boulder, CO 80305, USA  
E-mail: callie.higgins@nist.gov; jason.killgore@nist.gov

 The ORCID identification number(s) for the author(s) of this article can be found under <https://doi.org/10.1002/smt.201800275>.

DOI: 10.1002/smt.201800275

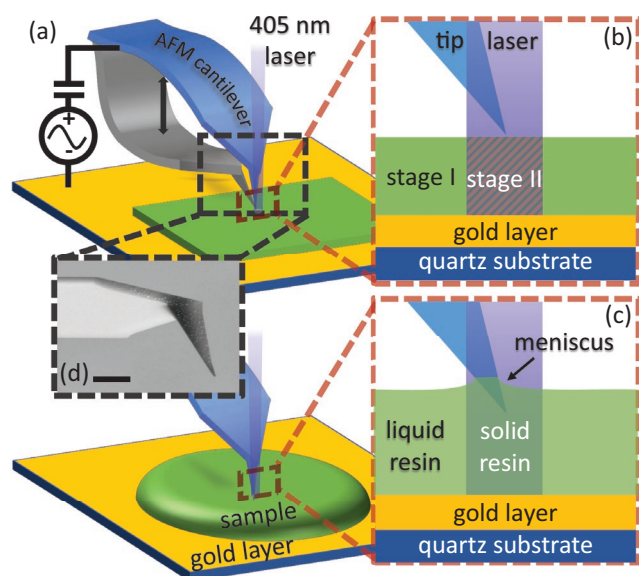


**Figure 1.** a) An illustration depicting the in situ SCRPR experiment on b) a sequential cure polymer and c) liquid resin. The cantilever's surface-coupled resonance is driven by an electrostatic force between the cantilever and gold substrate. Upon illumination with a 405 nm laser, the sample crosslinks from a rubbery stage I material (b) or liquid (c) to a glassy stage II material (b) or solid (c). The transformation of the material is continuously detected by the changing oscillator properties of the coupled cantilever. d) Scanning electron microscope image of ATEC probe; scale bar denotes 10  $\mu\text{m}$ .

AFM is well-equipped to measure local variations in as-printed part properties while offering a unique platform to develop voxel-scale in situ rheometry. AFM is touted for its exceptional spatial resolution, but the high-frequency microelectromechanical systems (MEMS) cantilever also provides inherently high temporal resolution for mechanical sensing.<sup>[9]</sup> We base our SCRPR measurement (Figure 1) off of contact resonance force microscopy, a dynamic AFM method that uses the resonance frequency  $f_n^c$  and quality factor  $Q_n^c$  of the  $n$ th eigenmode of a surface-coupled vibrating cantilever to determine the viscoelastic mechanical properties of the sample in question.<sup>[10]</sup> Both contact resonance force microscopy and SCRPR provide similar property information via analysis of the raw  $f_n^c$  and  $Q_n^c$  data with an Euler–Bernoulli beam model (Methods and Figure S2, Supporting Information). The principal difference is that contact resonance force microscopy is designed to measure  $f_n^c$  and  $Q_n^c$  at an instant in time across an array in space while the tip is coupled to the surface by contact mechanics, whereas SCRPR measures a single location in space across a finite timespan where the coupling may be contact (Figure 1b) or immersion (Figure 1c). For contact coupling, the spatial resolution of the in situ sensing is governed by the tip–sample contact radius, which can be as small as a few nanometers. For immersion coupling, the spatial resolution will be limited by the tendency of the fluid to wet the AFM tip, however sub-micrometer resolution should still be readily obtainable at shallow immersion depths. Because the tip is continually coupled to the surface, it is available for continuous sensing of mechanical property changes. The fundamental limit to the temporal resolution with which a cantilever can sense a changing force

and hence material property is given by the time constant  $\tau = Q_n^c / f_n^c$ . The value of  $f_n^c$  is higher than the frequency  $f_n^0$  for the  $n$ th mode of the freely vibrating cantilever and the quality factor  $Q_n^c$  on viscoelastic materials is much lower, giving the technique enhanced temporal resolution compared to quasi-static methods (e.g., force spectroscopy) or methods employing the free resonance of the cantilever (e.g., tapping mode). A typical contact resonance has a time constant between 10  $\mu\text{s}$  and 1 ms, allowing fast processes to be detected directly in the time domain. Even faster sensing is possible by employing higher eigenmodes of the cantilever<sup>[11]</sup> or using cantilevers with higher fundamental resonance frequency.<sup>[9a]</sup>

We performed SCRPR by adapting a commercial AFM (Asylum Research, Cypher) to use the 405 nm photothermal excitation laser, typically used to drive the cantilever,<sup>[12]</sup> to initiate photopolymerization at or near the tip–sample contact. The built-in laser allowed for precise synchronization of the polymerization initiation and the AFM detection mechanisms. Some requisites of the setup included a cantilever that did not shadow the tip–sample region from the 405 nm laser and a means of providing clean, periodic excitation to the cantilever. To address the former, an advanced tip at end of cantilever (ATEC) probe, where the tip extends past the cantilever body, was used for all experiments (Figure 1d). To address the latter, electrostatic excitation between the gold-plated cantilever body and a gold electrode that doubled as a sample substrate created the drive force. Initially, the first eigenmode ( $n = 1$ ) free resonance frequency ( $f_1^0$ ) and quality factor ( $Q_1^0$ ) of the cantilever were measured in air (Figure S3, Supporting Information). The tip was then lowered toward the sample of interest. Once the tip was coupled with the surface,  $f_1^c$  and  $Q_1^c$  were continuously measured using dual AC resonance tracking (DART) (Methods, Supporting Information).<sup>[13]</sup> After some delay, the exposure source (405 nm laser) was turned on while DART continued to track the changing  $f_1^c$  and  $Q_1^c$  throughout the polymerization reaction (Figure 1a–c, Figure S3, Supporting Information).

We first verified SCRPR on a sequential cure polymer (SCP) film. The SCP exhibits an initial rubbery modulus ( $\approx 2$  MPa, stage I), which crosslinks into a glassy modulus ( $\approx 1.5$  GPa, stage II) when irradiated with 405 nm light (Materials, Methods, and Figure S5, Supporting Information).<sup>[14]</sup> This material is an ideal proof-of-concept because it avoids the inherent complexities of the liquid-to-solid transition while still providing fast photorheological response. The two fundamental material characteristics investigated were polymerization timescales at high intensity exposures and photopolymerization reciprocity. Reciprocity, a common assumption made of light-based AM materials, is the concept that end material properties are independent of exposure power ( $P_e$ ) and exposure time ( $t_e$ ) if the total energy dose  $D_e = t_e P_e$  delivered to a fixed volume of material is kept constant (e.g., if  $t_{e1} = 1$  s and  $t_{e2} = 2$  s, then  $P_{e1} = 2$  mW and  $P_{e2} = 1$  mW should result in the same final material properties).<sup>[8]</sup>

The photopolymerization response of the SCP was tested by exposing it to four different exposure powers  $P_e = \{1, 2, 8, \text{ and } 12 \text{ mW}\}$  for respective exposure times  $t_e = \{450, 225, 56.25, \text{ and } 37.38 \text{ s}\}$ , thus maintaining the dose  $D_e = 450 \text{ mJ}$ . Figure 2a plots  $f_1^c$  and  $Q_1^c$  as functions of time for different exposure powers. Confirming the tip–sample coupling prior to exposure, the resonance frequency has increased from the free

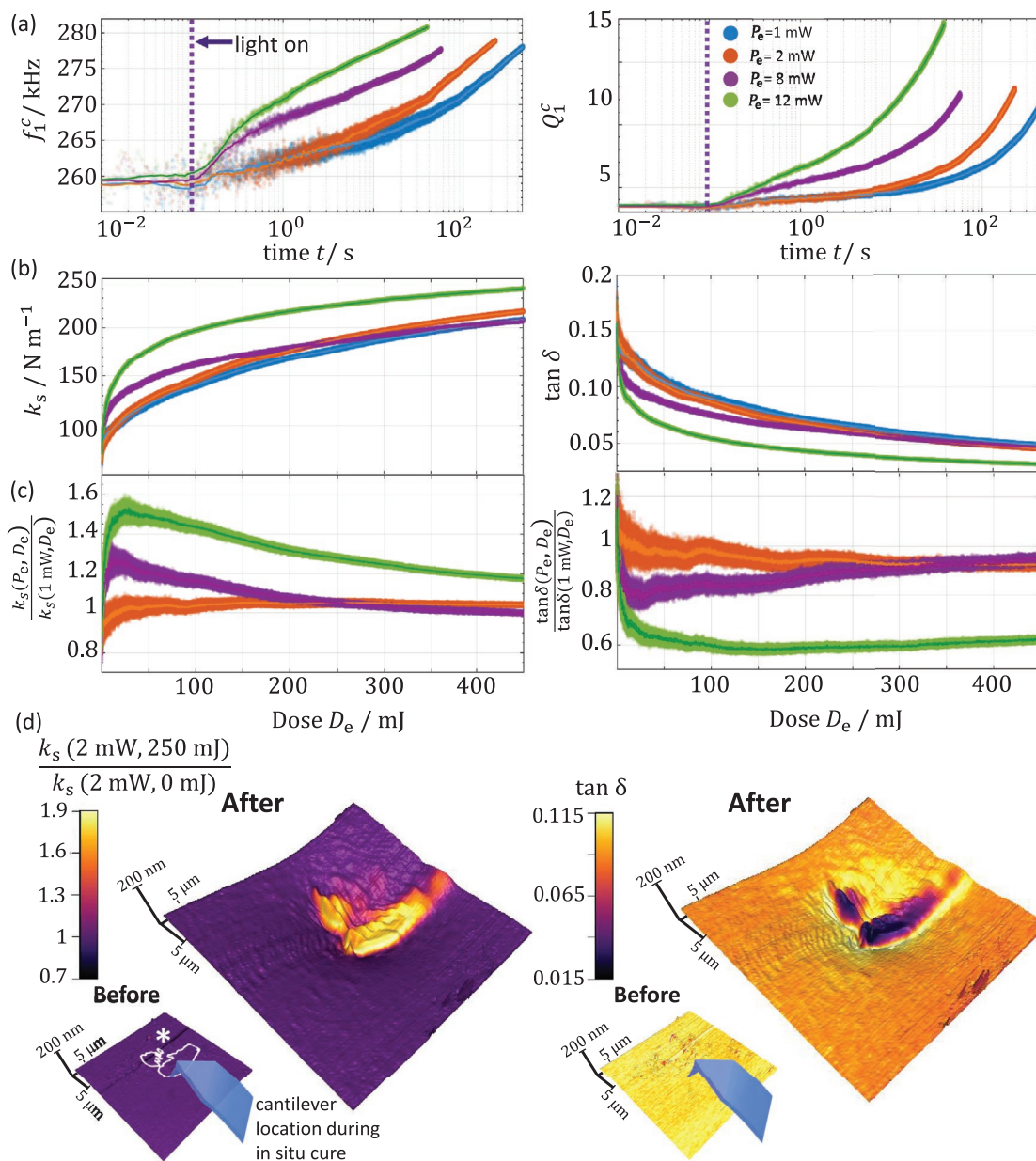


**Figure 2.** a) Sample-coupled-resonance frequency  $f_1^c$  and quality factor  $Q_1^c$  for the SCPs obtained at four different exposure powers,  $P_e = [1 \text{ mW (blue), } 2 \text{ mW (orange), } 8 \text{ mW (purple), and } 12 \text{ mW (green)]$ , plotted versus time on a logarithmic scale to illustrate the rapid photopolymerization reaction rate. Total exposure dose for each sample was held constant at  $D_e = 450 \text{ mJ}$  and the dotted purple line denotes  $t_e = 0$  exposure time. b) Contact stiffness  $k_s$  and loss tangent  $\tan \delta$  plotted versus dose for the four exposure powers and c)  $k_s$  and  $\tan \delta$  for each exposure power normalized by the  $P_e = 1 \text{ mW}$  exposure sample. d) 3D topographic images of the SCP before and after exposure with  $P_e = 2 \text{ mW}$ , overlaid with a color scale representing normalized  $k_s$  (normalized to the unpolymerized sample) and  $\tan \delta$ . The asterisk (\*) indicates the exposure spot outline. For all plots, the scatterplot points indicate actual data and the overlaid line indicates the moving average of said data.

value  $f_1^0 = 66.2 \text{ kHz}$  to contact values  $f_1^c \approx 259 \text{ kHz} \pm 1 \text{ kHz}$ . Upon exposure, the first result of note is that this technique has the unprecedented temporal resolution to capture the local, fast kinetic changes occurring during polymerization at each incident power (Figure 2a). The response time of the cantilever  $\tau$  is faster than  $50 \mu\text{s}$  throughout the measurements, and the lock-in amplifier time constants and sampling rate were adjusted accordingly. Significant changes in frequency at the onset of the 12 mW exposure can be observed over durations of  $\approx 5 \text{ ms}$ ,

introducing a practical estimate to the temporal resolution due to  $f_1^c$  and  $Q_1^c$  noise. When the light is turned on, shown by the purple dotted line, polymerization begins immediately, with the rate of  $f_1^c$  and  $Q_1^c$  increase depending monotonically on exposure power (Figure 2a). Whereas the 12 mW exposure achieves a 5 kHz increase in  $f_1^c$  in  $\approx 150 \text{ ms}$ , the 1 mW exposure requires 3 s to achieve an equivalent increase.

With sufficient temporal resolution to resolve the cure demonstrated, the data were assessed to determine whether

reciprocity was maintained during the exposures. It is immediately apparent that reciprocity is an invalid assumption at the highest intensity based on the differing final  $f_1^c$  and  $Q_1^c$  for the 12 mW exposure compared to the 8, 2, and 1 mW exposures, which have equivalent  $f_1^c$  and  $Q_1^c$  within 7%. (Figure 2a). To elucidate this phenomenon further, the tip-sample contact stiffness  $k_s$  and loss tangent  $\tan \delta$  were calculated using the characteristic equation for the surface-coupled beam (Methods, Supporting Information) and plotted versus exposure dose, which was equivalent for each exposure (Figure 2b). The values of  $k_s$  and  $\tan \delta$  allow for comparison with bulk stage I and II properties determined from dynamic mechanical analysis (DMA, Figure S1, Supporting Information). Because of the five orders of magnitude higher frequencies in SCRPR, Williams-Landall-Ferry (WLF)-like behavior is assumed<sup>[15]</sup> and the comparison is made to low frequency (i.e., 1 Hz) bulk DMA data at 30–40 °C lower temperature than the ambient SCRPR. From bulk DMA, we estimate frequency-corrected stage I properties as  $E'(I) = (320 \pm 180)$  MPa and  $\tan \delta(I) = 0.6 \pm 0.4$  and stage II properties as  $E'(II) = (2.1 \pm 0.1)$  GPa and  $\tan \delta(II) = 0.046 \pm 0.003$ . The bulk  $\tan \delta$  values can be compared to the SCRPR values, and indicate good to excellent agreement. In stage I, SCRPR measures  $\tan \delta \approx 0.15$ , which is slightly below the DMA's mean  $\tan \delta$  between  $-20$  and  $-10$  °C, but agrees perfectly with DMA values at  $-20$  °C. For stage II, SCRPR measures  $\tan \delta = 0.05$ , agreeing well with the bulk value. The simpler comparison of data for stage II is a result of the glass transition temperature shifting to higher values at the higher crosslink density. This ensures that the stage II material is fully into the glassy plateau at temperatures less than  $-10$  °C compared to the stage I material which is in the glass transition peak and thus very sensitive to slight changes in temperature and frequency and deviations from ideal WLF behavior. The relative increase in  $k_s$  predicted from the bulk properties is determined by assuming Hertzian contact wherein

$$\frac{k_s(II)}{k_s(I)} = \left( \frac{E'(II)}{E'(I)} \right)^{3/2} = \left( \frac{2.1 \text{ GPa}}{0.32 \text{ GPa}} \right)^{3/2} = 3.5 \quad (1)$$

For the 12 mW SCRPR exposure, we observe  $k_s(II)/k_s(I) = 3.4$  whereas 1, 2, and 8 mW exposures yield  $k_s(II)/k_s(I) = 2.9$ . Overall, from stiffness and damping changes it appears that during SCRPR, the SCP is achieving bulk-like conversion, with the highest conversion in the case of the 12 mW intensity.

To compare the in situ variations in reciprocity versus dose,  $k_s$  and  $\tan \delta$  for the 2, 8, and 12 mW power exposures were normalized by the respective values for  $P_e = 1$  mW as shown in Figure 2c. Comparing normalized  $k_s$  and  $\tan \delta$  for the  $P_e = 2$  mW and 8 mW cases results in nearly equivalent end-of-cure properties, but the path by which the SCP came to that state is drastically different and power-dependent. Thus, Figure 2c proves that end-of-cure reciprocity is not indicative of reciprocity being valid throughout exposure. By considering the relative changes in  $k_s$  as an indication of degree of cure, the polymerization rates as a function of dosage between the different exposure powers can be compared. Assuming a first-order reaction, for the initial 100 mJ of exposure, 1 and 2 mW power give equivalent rate, 8 mW exposure is a factor of two

faster, and 12 mW power is more than three times faster. Fitting over the entire 450 mJ exposure, the 8 mW case slows to be back in agreement with 1 and 2 mW exposures, whereas the 12 mW case remains three times faster. The normalized property changes during cure and kinetic data can be combined with post-cure contact resonance maps of  $k_s$  and  $\tan \delta$  of the printed stage II spots (Figure 2d) to provide insight into the mechanism for nonreciprocity. The spatial property maps indicate a remarkably sharp interface at the edge of the illumination, suggesting that long range lateral diffusion of species (e.g., initiated free radicals) was negligible and thus an unlikely source of the observed nonreciprocity. In these experiments it seems probable that the increased rate after normalizing for dosage is attributed to the local heating of the sample. Local heating may lower the relative energy barrier for photo-initiation,<sup>[16]</sup> directly crosslink the material, or result in thermal degradation. These results indicate that for polymerizations engineered to have variable dose throughout an exposure voxel, the final properties can vary in an unpredictable manner unless characterized using an in situ technique at the relevant power. Shifting from a solid-to-solid photopolymerization to one exhibiting liquid-to-solid transformation presents even greater opportunity for nonreciprocity as diffusion rates in the liquid state are considerably higher.

Having demonstrated the utility of the SCRPR on a model material system, we next investigated its ability to characterize the photorheology of the liquid-to-solid cure of a commercial SLA resin (FSL3D Universal Clear Resin). The experimental setup and design for the SCP were repeated except that the solid SCP material was replaced with liquid resin on the gold-plated substrate (Figure 1c). The free resonance  $f_1^0$  was similarly obtained prior to contacting the liquid resin. Unlike the contact-coupling with SCP, to characterize the resin-coupled resonance, the tip was lowered into the 4–5  $\mu\text{m}$  thin resin layer until the tip contacted the gold substrate and was then retracted 3  $\mu\text{m}$ , leaving the tip 1–2  $\mu\text{m}$  immersed in the resin. The coupled cantilever was then driven electrostatically to assess the immersion-coupled resonance frequency  $f_1^c$ . Notably,  $f_1^c = 69.5$  kHz of the cantilever coupled to the liquid commercial resin was shifted to a significantly higher frequency than  $f_1^0 = 13.1$  kHz (Figure 3a and Figure S5, Supporting Information). This effect is indicative of a meniscus force contribution to the coupled tip-resin interaction. The meniscus force increases the resonance frequency when the tip is immersed because the surface tension in the resin creates a spring-like response, which we verified by its similarity to the response of a known Newtonian fluid (i.e., no possibility of elastic forces) (Figure S6, Supporting Information).<sup>[17]</sup> The uncharacterized meniscus force contribution complicates quantification of the material properties of the resin surrounding the tip (Figure 1c). Modeling and minimizing the meniscus force contribution to the measurement is critical to extracting quantitative material properties from this in situ technique and is thus the subject of future work. Nonetheless, the presence of a background meniscus stiffness does not preclude the possibility of detecting a relative change in coupled stiffness and damping for the resin upon photopolymerization, thus indicating reaction timescale and qualitative indications of stiffness and damping evolution.

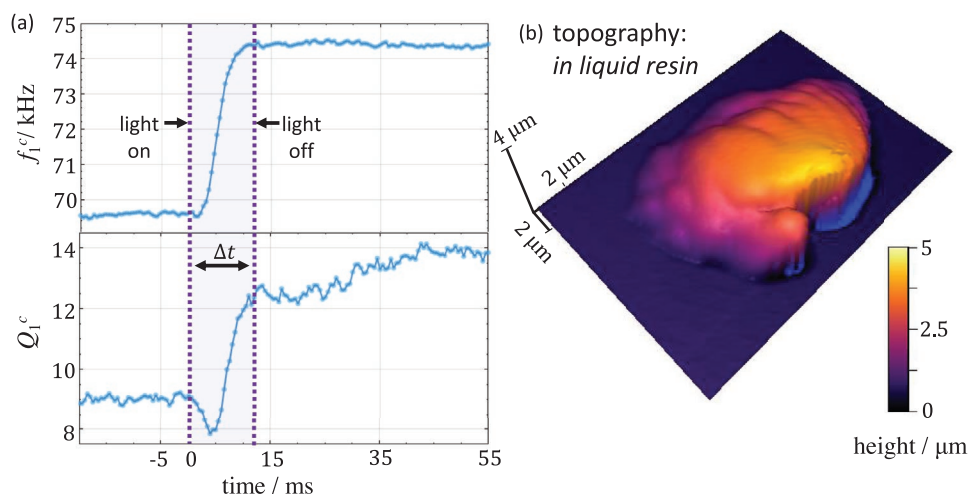


**Figure 3.** a) The resin-coupled resonance frequency  $f_1^c$  and quality factor  $Q_1^c$  captured during a 12 ms, 405 nm laser exposure on a commercial SLA resin. The shaded purple region between the purple dotted lines denotes exposure duration. b) A 3D topographic image of the polymerized voxel swollen-with and surrounded-by unpolymerized liquid resin. This configuration is representative of the native SLA 3D printing environment.

As shown by the  $f_1^c$  and  $Q_1^c$  changes versus time in Figure 3a, SCRPR senses fast, local property changes throughout liquid-to-solid polymerization with unprecedented temporal resolution ( $<0.5$  ms) for photorheological characterization. Though this result is not converted to material properties yet, it remains the first demonstration of the ability to capture the polymerization of a commercially available resin with sufficient spatiotemporal resolution at AM-relevant exposure powers. It follows that the detected frequency increase is attributed to one or both of (1) the meniscus stiffness is increasing due to changing surface tension in the resin or (2) the elastic stiffness of the resin coupled to the tip is increasing due to polymerization.

To confirm that liquid-to-solid polymerization had occurred during the exposure, the voxel was imaged after in situ characterization. Force–volume mapping was used to image the swollen voxel while still immersed in surrounding monomer (Methods, Supporting Information). A topographic image of the cured voxel is shown in Figure 3b. The solid structure shows that polymerization has taken place. Again, the printed structure coincides well with the aberrant laser focus, enabling the correlation between incident exposure intensity and as-printed feature development. Because the chemical structure and density do not change significantly during polymerization, we do not have evidence to suggest that a changing meniscus force is dominant. Thus, the increase in  $f_1^c$  during exposure is attributed primarily to an increased elasticity in the coupled resin from polymerization. Furthermore, the nonmonotonic relationship between  $Q_1^c$  and time (i.e., the slight dip immediately after initial exposure) indicates a peak in dissipation, which may correspond with gelation or the glass transition. This result lays the groundwork for more complex measurements that shift the sensing tip laterally and vertically to probe the complete 3D voxel formation, and with a more sophisticated exposure source, even simultaneous voxel–voxel interactions could be probed.

In summary, SCRPR affords the first in situ measurements of local, fast rheological changes in both a model, sequential cure polymer and a commercial 3D printing resin with

sub-micrometer spatial and millisecond temporal resolution. Compared to bulk rheological techniques, this represents orders of magnitude improvement in spatially and temporally resolved rheological measurements. SCRPR was capable of definitively disproving assumptions of reciprocity in the SCP system, while revealing shortcomings associated with making such assumptions based purely on single-dose, as-printed property measurements. Liquid-to-solid polymerization, such as that exhibited by the commercial 3D printing resin, is a more complex chemical reaction, with greater potential for species diffusion, suggesting even stricter limits on the assumption of reciprocity. Nonetheless, SCRPR can probe the liquid-to-solid polymerization and then subsequently image the monomer-swollen voxel in its native environment. Moving forward, SCRPR can be adapted to utilize a broader range of polymerization sources through either top-down, or bottom-up illumination, expanding the classes of photoresponsive materials than can be studied. Likewise, recent contact resonance force microscopy advancements could be leveraged to study photomechanical response in liquids<sup>[18]</sup> or to enhance the stiffness sensitivity of the method to broader stiffness ranges and improve temporal resolution with higher eigenmodes.<sup>[11]</sup> Overall, SCRPR allows researchers to understand changes in rheological properties of photopolymerizable materials throughout the duration of cure, providing a critical measurement capability for optimizing fast and/or small-scale polymerization processes such as 3D printing, dental composites, and coatings.

## Supporting Information

Supporting Information is available from the Wiley Online Library or from the author.

## Acknowledgements

Specific commercial instruments and materials that are identified in this manuscript are listed to adequately describe the experimental procedure

and are not intended to imply endorsement or recommendation by the National Institute of Standards and Technology (NIST). Contribution of NIST, an agency of the U.S. government; not subject to copyright.

## Conflict of Interest

The authors declare no conflict of interest.

## Keywords

additive manufacturing, AFM, contact resonance, photopolymerization, rheology

Received: August 1, 2018

Revised: September 7, 2018

Published online: October 4, 2018

- [1] a) B. Berman, *Bus. Horiz.* **2012**, *55*, 155; b) H. Cui, M. Nowicki, J. P. Fisher, L. G. Zhang, *Adv. Healthcare Mater.* **2017**, *6*, 1601118; c) J. Jang, H.-G. Yi, D.-W. Cho, *ACS Biomater. Sci. Eng.* **2016**, *2*, 1722; d) M. S. Mannoor, Z. Jiang, T. James, Y. L. Kong, K. A. Malatesta, W. O. Soboyejo, N. Verma, D. H. Gracias, M. C. Mcalpine, *Nano Lett.* **2013**, *13*, 2634; e) F. P. W. Melchels, J. Feijen, D. W. Grijpma, *Biomaterials* **2010**, *31*, 6121.
- [2] a) P. J. Bártolo, *Stereolithography*, Springer, Berlin **2011**, pp. 209–241; b) P. F. Jacobs, *Rapid Prototyping & Manufacturing: Fundamentals of Stereolithography*, Society of Manufacturing Engineers, South Field, MI **1992**; c) G. D. Kim, Y. T. Oh, *Proc. Inst. Mech. Eng., Part B* **2008**, *222*, 201; d) S. Mansour, M. Gilbert, R. Hague, *Mater. Sci. Eng., A* **2007**, *447*, 277; e) M. Monzón, Z. Ortega, A. Hernández, R. Paz, F. Ortega, *Materials* **2017**, *10*, 64; f) W. L. Wang, C. M. Cheah, J. Y. H. Fuh, L. Lu, *Mater. Des.* **1996**, *17*, 205.
- [3] a) J. Stampfl, S. Baudis, C. Heller, R. Liska, A. Neumeister, R. Kling, A. Ostendorf, M. Spitzbart, *J. Micromech. Microeng.* **2008**, *18*, 125014; b) M. Agarwala, D. Bourell, J. Beaman, H. Marcus, J. Barlow, *Rapid Prototyping J.* **1995**, *1*, 26; c) T. Billiet, M. Vandenhaute, J. Schelfhout, S. Van Vlierberghe, P. Dubruel, *Biomaterials* **2012**, *33*, 6020; d) Q. Gao, Z. Liu, Z. Lin, J. Qiu, Y. Liu, A. Liu, Y. Wang, M. Xiang, B. Chen, J. Fu, Y. He, *ACS Biomater. Sci. Eng.* **2017**, *3*, 399; e) S. Hong, J. Yeo, G. Kim, D. Kim, H. Lee, J. Kwon, H. Lee, P. Lee, S. H. Ko, *ACS Nano* **2013**, *7*, 5024.
- [4] a) I. Sakellari, E. Kabouraki, D. Gray, V. Purlys, C. Fotakis, A. Pikulin, N. Biturur, M. Vamvakaki, M. Farsari, *ACS Nano* **2012**, *6*, 2302; b) G. Zhao, P. Mouroulis, *J. Mod. Opt.* **1994**, *41*, 1929.
- [5] C. M. Cheah, A. Y. C. Nee, J. Y. H. Fuh, L. Lu, Y. S. Choo, T. Miyazawa, *J. Mater. Process. Technol.* **1997**, *67*, 41.
- [6] K. Chockalingam, N. Jawahar, U. Chandrasekhar, *Rapid Prototyping J.* **2006**, *12*, 106.
- [7] A. Zgrzeba, E. Andrzejewska, A. Marcinkowska, *RSC Adv.* **2015**, *5*, 100354.
- [8] a) S. C. Ligon, R. Liska, J. Stampfl, M. Gurr, R. Mülhaupt, *Chem. Rev.* **2017**, *117*, 10212; b) A. Maffezzoli, R. Terzi, *Thermochim. Acta* **1998**, *321*, 111; c) B. D. Mather, K. Viswanathan, K. M. Miller, T. E. Long, *Prog. Polym. Sci.* **2006**, *31*, 487.
- [9] a) T. Ando, T. Uchihashi, N. Kodera, *Annu. Rev. Biophys.* **2013**, *42*, 393; b) R. Giridharagopal, G. E. Rayermann, G. Shao, D. T. Moore, O. G. Reid, A. F. Tillack, D. J. Masiello, D. S. Ginger, *Nano Lett.* **2012**, *12*, 893.
- [10] a) J. P. Killgore, F. W. Delrio, *Macromolecules* **2018**, *51*, 6977; b) D. C. Hurley, S. E. Campbell, J. P. Killgore, L. M. Cox, Y. Ding, *Macromolecules* **2013**, *46*, 9396; c) J. P. Killgore, D. G. Yablon, A. H. Tsou, A. Gannepalli, P. A. Yuya, J. A. Turner, R. Proksch, D. C. Hurley, *Langmuir* **2011**, *27*, 13983; d) U. Rabe, *Applied Scanning Probe Methods II*, Springer, Berlin **2006**, pp. 37–90; e) P. A. Yuya, D. C. Hurley, J. A. Turner, *J. Appl. Phys.* **2011**, *109*, 113528.
- [11] a) J. A. Turner, J. S. Wiehn, *Nanotechnology* **2001**, *12*, 322; b) J. P. Killgore, D. C. Hurley, *Nanotechnology* **2012**, *23*, 055702.
- [12] M. Kocun, A. Labuda, A. Gannepalli, R. Proksch, *Rev. Sci. Instrum.* **2015**, *86*, 083706.
- [13] B. J. Rodriguez, C. Callahan, S. V. Kalinin, R. Proksch, *Nanotechnology* **2007**, *18*, 475504.
- [14] D. P. Nair, N. B. Cramer, J. C. Gaipa, M. K. McBride, E. M. Matherly, R. R. Mcleod, R. Shandas, C. N. Bowman, *Adv. Funct. Mater.* **2012**, *22*, 1502.
- [15] R. Lakes, *Viscoelastic Materials*, Cambridge University Press, Cambridge **2009**.
- [16] W. D. Cook, S. Chausson, F. Chen, L. Le Pluart, C. N. Bowman, T. F. Scott, *Polym. Int.* **2008**, *57*, 469.
- [17] a) A. Abdi, H. N. Pishkenari, R. Keramati, M. Minary-Jolandan, *Nanotechnology* **2015**, *26*, 205702; b) C. Jai, J. P. Aimé, D. Mariolle, R. Boisgard, F. Bertin, *Nano Lett.* **2006**, *6*, 2554.
- [18] A. B. Churnside, R. C. Tung, J. P. Killgore, *Langmuir* **2015**, *31*, 11143.